Alma Mater Studiorum Università di Bologna
Archivio istituzionale della ricerca

LOS/NLOS Near-Field Localization with a Large Reconfigurable Intelligent Surface

(Article begins on next page)

Terms of use:

LOS/NLOS Near-Field Localization with a Large Reconfigurable Intelligent Surface

Davide Dardari, *Senior Member, IEEE*, Nicoló Decarli, *Member, IEEE*,
Anna Guerra, *Member, IEEE*, Francesco Guidi, *Member, IEEE*

Abstract—This paper considers a scenario where a reconfigurable intelligent surface (RIS) is deployed to allow the localization of mobile users adopting a single anchor node, even under non-line-of-sight (NLOS) channel conditions. When the RIS is large and the operating frequency is high, as in the millimeter-wave band, the system is likely to operate in the near-field propagation regime, which can be exploited to obtain robust localization. To this purpose, two practical signaling and positioning algorithms, based on an orthogonal frequency division multiplexing (OFDM) downlink system, are proposed along with methods to design the RIS time-varying reflection coefficients. In the numerical results, the two algorithms are compared in terms of performance in the presence of a synchronization mismatch and considering trade-offs between bandwidth, overhead, operating frequency, and latency. Finally, we provide an analysis of the soft-coverage capability, i.e., on the possibility of maintaining a high level of localization accuracy when in the presence of increasing levels of obstruction of the RIS.

Index Terms—Holographic localization, reconfigurable intelligent surfaces, near-field positioning, NLOS, OFDM

I. INTRODUCTION

STARTING from fifth-generation (5G) wireless networks, localization has become a by-design and essential feature which is fundamental not only to enable new location-aware services but also to assist communication tasks. Recently, the focus of research has shifted to next-generation wireless networks (6G) that are expected to be characterized by very stringent requirements in terms of localization accuracy, reliability, and latency [1]. The adoption of new frequency bands at millimeter-wave (mmWave) and terahertz guarantees higher available bandwidths, corresponding to potentially higher positioning accuracies [2]–[5] but, at the same time, it opens up new challenges in terms of coverage and reliability because signals can be blocked by obstacles and the multipath may not be sufficient to guarantee a suitable coverage in non-line-of-sight (NLOS) channel conditions. In this context, the main question becomes how to ensure an ultra-reliable localization and communication in harsh propagation environments, such as in industrial Internet of Things (IoT) applications, without

a massive and costly deployment of base stations (BSs) (i.e., cell densification).

A promising technology to tackle this problem is represented by metasurfaces made up of metamaterials, which allow the realization of programmable intelligent surfaces offering a high degree of flexibility in managing the electromagnetic (EM) field. Initially introduced to boost the communication performance in terms of coverage and channel rank improvement, active and passive intelligent surfaces have also been proposed to enhance the localization of mobile user equipments (UEs) in the presence of only one BS (often called *anchor node*). Indeed, active intelligent surfaces can be successfully adopted to realize very large antennas allowing single-anchor localization by exploiting the wavefront curvature occurring in (radiating) near-field propagation conditions, as investigated in [6], [7], thus extending the results already available for traditional large antenna arrays [8]–[10]. In order to reduce the complexity, very large antennas can also be realized by combining a passive intelligent surface acting as a lens and a single antenna forming a transmitarray configuration [7], [11]. On the other hand, single-anchor localization can also be achieved by deploying passive reflecting reconfigurable intelligent surfaces (RISs) [12]. Nevertheless, improving localization by leveraging passive reflecting cells is not new. In [13], ultrawide bandwidth (UWB) passive relays were introduced to generate artificial multipath which can be exploited to allow positioning when the number of visible anchor nodes is not sufficient to infer the position of the mobile UE. Following a similar philosophy, the authors in [14]–[16] proposed the exploitation of natural specular reflections caused by the environment in order to generate "virtual anchors" providing position information from different points of views.

Centimeter-level accuracy has been demonstrated theoretically and experimentally in [17]–[19] using passive UWB-radio frequency identification (RFID) tags whose reflection properties change with time according to some unique sequences (backscatter modulation). The way each tag works is similar to that of each cell of a RIS. In fact, in both cases, the reflection coefficient is dynamically changed to allow the extraction of the tag/cell-reflected signal component that can be exploited for localization. The authors in [17]–[19] have shown that, by properly designing the sequences and processing schemes, it is possible to isolate the signal component of each tag from the dominant clutter generated by the surrounding environment, thus allowing reliable detection and precise ranging by measuring the round-trip time of the signal. Thanks to this similarity, some solutions designed for

UWB-RFID tags can be adapted and successfully applied to a RIS as well, as done in Sec. III.

More recently, scenarios with RIS-assisted localization have been considered, as already mentioned, where the signal emitted by a BS is reflected in a controlled manner by the RIS and then exploited to localize a UE [12]. In some sense, RIS-based localization can be seen as the fusion of the aforementioned approaches, where each cell of the RIS employs backscatter modulation and the reflected signals are considered to be generated by intelligent virtual anchors. In this context, some papers have focused on the derivation of fundamental limits. Specifically, in [20] the position error bound (PEB) is derived in an uplink scenario showing the improvement of the localization accuracy obtainable when a RIS is present. In [21], the Cramér-Rao bound (CRB) has been examined in an uplink scenario where a single-antenna UE sends a UWB signal which is received by a multi-antenna BS. The BS takes advantage of the time resolution offered by the UWB signals to discriminate the signal components coming from the cells of the RIS. The authors in [22] investigate in terms of CRBs in a downlink scenario the advantage of RISs over schemes that exploit only the natural scattering of the environment. A similar scenario is analyzed in [23], where the position and the orientation error bounds are derived in a multiple-input multiple-output (MIMO) configuration.

Some practical RIS-aided localization algorithms can be found in [24]–[28]. In [24], [25], a received signal strength (RSS)-based multi-user positioning scheme is proposed in which the phase profile of the RIS' cells is optimized to obtain a favorable RSS distribution in space, and thus better discrimination of the RSS signature of neighboring locations. In [26], a machine learning method for RSS-based finger-print localization is investigated. The authors demonstrate that the diversity offered by RISs can be successfully used to generate reliable radio maps. Although RSS-based techniques require simple hardware, in general they do not provide the same performance as schemes that take full advantage of the characteristics of the received signal. The authors in [27], [28] consider a single-input single-output (SISO) orthogonal frequency division multiplexing (OFDM) downlink scenario with a RIS in far-field regime. Starting from the derivation of the PEB, they propose a low-complexity localization algorithm that estimates the time-of-arrival (TOA) of the direct path and the path reflected by the RIS, as well as the angle-of-departure from the RIS, to infer the position of the UE also considering the synchronization mismatch. The estimation of signal delays is obtained by accumulating a large number of pilot symbols and considering a random phase configuration of RIS' cells, as also proposed in some RIS-aided channel state information (CSI) estimation algorithms (see, for example, [29]).

The main limitation of previous literature on localization algorithms is that the RIS is considered in the far-field propagation regime with respect to the BS and UE, thus simplifying the problem because only a couple of parameters is sufficient to describe its reflection capability. Indeed, the proposed schemes require the visibility of the BS from the UE to compare the signal reflected by the RIS with that received directly from the BS. Furthermore, the component

of the signal reflected by natural scatterers (clutter), which may be dominant with respect to the signals reflected by the RIS, especially in the presence of metal, is often neglected in the analysis. To implement practical localization systems, it is of interest the design of localization algorithms capable of providing satisfactory performance when the UE and the BS are in NLOS, and with a RIS partially obstructed with respect to the UE. Moreover, an analysis of the trade-offs between bandwidth, overhead, and latency in RIS-aided localization is still missing to the best of the authors' knowledge.

In this paper, we consider the problem of single-anchor localization assisted by RIS, where a large RIS is used to address the issue of coverage in scenarios characterized by frequent NLOS conditions. Unlike the situations studied in previous papers, where RISs are assumed to work in far-field conditions with respect to BS and UE positions, here the presence of a large RIS makes the far-field hypothesis no longer valid at practical distances and at high frequencies. For instance, the Fraunhofer distance, which conventionally determines the boundary between the (radiating) near- and far-field regions [30], is approximatively $2 \cdot 10^3$ m and $19 \cdot 10^3$ m at 3 GHz and 28 GHz, respectively, for a RIS of size $D = 10$ m. Therefore, indoor positioning systems are expected to operate primarily in the near-field propagation regime.[1] Although the near-field condition renders most of the previously-proposed positioning approaches not applicable, it opens up new opportunities to localize the UE even under NLOS conditions providing a soft-coverage capability, i.e., the maintenance of high localization accuracy with different levels of obstruction of the RIS, as will be investigated in this paper. In this context, we propose two methods of signaling and positioning, characterized by different complexity, performance, latency, and overhead requirements. Both approaches can work with an asynchronous OFDM SISO system in the presence of a synchronization mismatch, under NLOS conditions, and with a potentially unlimited number of UEs since the localization process relies on downlink signals only. The first positioning method works with both narrowband and wideband signals, whereas the second only works with wideband signals.

To exploit the near-field condition, an electrically large RIS is needed. However, in a typical scenario where the required positioning is almost 2D, it is sufficient that the RIS is large only in one dimension. Therefore, for a fixed area (i.e., cost) of the RIS, a stripe-like RIS, briefly referred to as *linear RIS*,[2] is more appealing than a conventional square-shape RIS. In addition, a linear RIS allows for an easier deployment along the room's perimeter than a planar RIS which might occupy large portions of the wall. Compared to the situation typically faced in which one or more squared RISs are considered, the adoption of a large linear RIS has the advantage to reduce the possibility that the whole RIS is completely obstructed by obstacles with respect to the BS and UE, thus leading to a

---

[1] A more accurate investigation of the near-field condition for localization goes beyond the definition of the Fraunhofer distance, as investigated in [6]–[10].

[2] In this paper, we use the term *linear* for convenience only, although the RIS is not mono-dimensional, but simply to denote that its height is much smaller than its width.
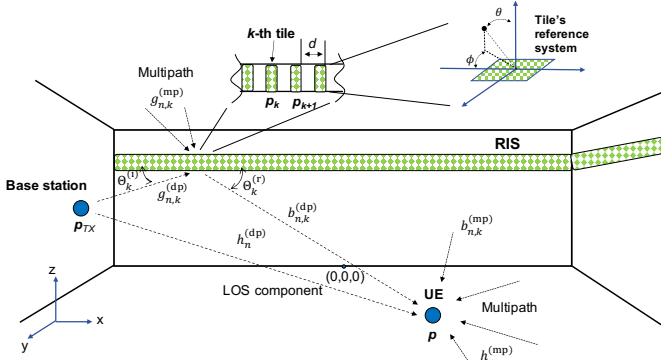
Fig. 1.   Scenario employing a large RIS.

soft-coverage capability with reduced area, as it will be presented in this paper. For these reasons, although the proposed solutions apply to RISs of any shape, we focus our numerical investigations on large linear RISs. In the numerical results, the trade-off between bandwidth (number of subcarriers) and the number of pilot symbols (i.e., OFDM symbols) dedicated to positioning is examined, which indirectly provides the trade-off between the overhead for positioning and latency. Comparisons in terms of design strategies of RIS coefficients and carrier frequencies are shown to illustrate their effect and impact on localization accuracy and coverage. Finally, the analysis of the soft-coverage capability is provided.

The remainder of this paper is organized as follows. In Sec. II, the models of the RIS, the channel, and the OFDM-based system are described. The properties of the RIS coefficients required to allow the extraction of the signal components related to the direct link, multipath, and RIS tiles, are introduced in Sec. III. In Sec. IV and Sec. V, a direct and two-step positioning algorithms exploiting the various signal components are proposed. For comparison, theoretical performance bounds are derived in Sec. VI. Numerical results and discussions are presented in Sec. VII. Finally, conclusions are drawn in Sec. VIII.

II. System Model

With reference to Fig. 1, we consider an OFDM SISO system where one BS, located in position $\mathbf{p}_{\text{TX}}$, acts as transmitter (TX) and one mobile UE as receiver (RX) that aims to estimate its own position $\mathbf{p}$ by exploiting the presence of a RIS synchronized with the BS. To accomplish this task, the BS sends T OFDM pilot symbols $\{x_{t,n}\}$, with $t = 1, 2, \ldots, T$ and $n = 1, 2, \ldots, N$, where N denotes the number of subcarriers used by the pilot symbols out of a total number of subcarriers N_{t}. The generic subcarrier n has frequency $f_n = f_{\text{c}} + (n - (N+1)/2)\Delta f$, $n = 1, 2, \ldots, N$, with f_{c} being the carrier frequency, and Δf the subcarrier spacing.

The RIS consists of K tiles located in known positions $\mathbf{p}_k$, $k = 1, 2, \ldots, K$, each of them composed of N_{e} sub-wavelength unit cells arranged to form a planar array of $N_x \times N_y$ cells of size $A_{\text{t}} = L_x \times L_y$ with spacing d_x and d_y, respectively. The organization of a RIS in tiles follows the approach proposed in [31] to make large RISs optimization scalable so that

the number of parameters to be optimized and hence the implementation complexity of the RIS are reduced. If the EM wavefront can be approximated as plane within the area of each tile, then the flexibility of the RIS to transform the impinging EM wave is not significantly compromised with respect to a RIS where all the cells are programmed independently [31]. Accordingly, we suppose that the phase of the reflection coefficient of each tile (common to all its cells) can be programmed independently from the other tiles and can be dynamically modified during the reflection of the pilot symbols according to some predefined sequence that will be specified in Sec. VII. In particular, considering each tile (but not the entire RIS in general) in far-field condition, the reflection coefficient at time $t \in \{1, 2, \ldots T\}$ of tile $k \in \{1, 2, \ldots K\}$, in the presence of an incident plane wave with 3D angle $\Theta_k^{(\text{i})} = \left(\theta_k^{(\text{i})}, \phi_k^{(\text{i})}\right)$ and observed at angle $\Theta_k^{(\text{r})} = \left(\theta_k^{(\text{r})}, \phi_k^{(\text{r})}\right)$, is modeled as[3] [31]–[33]

$$\beta_{t,k} = \sqrt{F\left(\Theta_k^{(\text{i})}\right) F\left(\Theta_k^{(\text{r})}\right)} \, \text{AF}\left(\Theta_k^{(\text{i})}\right) \text{AF}\left(\Theta_k^{(\text{r})}\right) G_{\text{c}} \, e^{J\Psi_{t,k}} \quad (1)$$

where

$$\text{AF}(\Theta) = \frac{1}{\sqrt{N_{\text{e}}}} \frac{\sin\left(\frac{\pi N_x d_x}{\lambda} \sin\theta \sin\phi\right)}{\sin\left(\frac{\pi d_x}{\lambda} \sin\theta \sin\phi\right)} \cdot \frac{\sin\left(\frac{\pi N_y d_y}{\lambda} \sin\theta \cos\phi\right)}{\sin\left(\frac{\pi d_y}{\lambda} \sin\theta \cos\phi\right)} \tag{2}$$

is the array factor of the tile [30], [31], $F(\Theta)$ is the normalized power radiation pattern that accounts for the non-isotropic behavior of the single cell of the tile, G_{c} is the boresight cell gain, $\Psi_{t,k}$ is the reflection phase, $\lambda = c/f_{\text{c}}$ is the wavelength and c is the speed of light. For instance, in [33], [34] the following parametric shape for $F(\Theta)$ is considered

$$F(\Theta) = \begin{cases} \cos^q(\theta) & \theta \in [0, \pi/2], \phi \in [0, 2\pi) \\ 0 & \text{otherwise} \end{cases} \tag{3}$$

where parameter q depends on the specific technology as well as on the size of the cell, and it is related to the boresight gain $G_{\text{c}} = 2(q+1)$. Following an approach similar to that in [33], one possibility is to set G_{c} so that the effective area of the cell is equal to its geometric area A_{c}, i.e., $G_{\text{c}} = A_{\text{c}} 4\pi/\lambda^2$, assuming an ideal radiation efficiency. Considering, for instance, a cell with square area $A_{\text{c}} = (\lambda/2)^2$, it follows that $G_{\text{c}} = \pi \simeq 5$ dBi, and $q = 0.57$. Regarding the reflection phase $\Psi_{t,k}$, in the numerical results we will consider the ideal case where it can take any value in the range $[0, 2\pi)$, and a more practical case where it can take only the binary values $\{0, \pi\}$.

The (complex) coefficient representing the direct channel between the TX and the UE for subcarrier n is indicated as

$$h_n^{(\text{d})} = h_n^{(\text{dp})} + h_n^{(\text{mp})} \tag{4}$$

where $h_n^{(\text{dp})}$ is the direct path component, different from zero when the UE is in line-of-sight (LOS) with respect to the BS,

---

[3]We adopt the conventional spherical coordinate system centered at the tile, where $\phi \in [0, 2\pi)$ (azimuth) and $\theta \in [0, \pi)$ (inclination), with respect to the plane of the tile, as shown in Fig. 1.

and $h_n^{(\text{mp})}$ is the multipath component. Specifically, the direct path component is given by

$$h_n^{(\text{dp})} = \xi_0 \frac{\sqrt{G_{\text{T}}\,G_{\text{R}}\,P_{\text{T}}/N_{\text{t}}}\,\lambda_n}{4\pi\,\|\mathbf{p}_{\text{TX}} - \mathbf{p}\|}$$
$$\cdot \exp\left(-j\frac{2\pi f_n}{c}\,\|\mathbf{p}_{\text{TX}} - \mathbf{p}\| + j2\pi f_n t_0 + j\phi_0\right) \quad (5)$$

where t_0 and ϕ_0 are the clock and phase offset between the TX and RX, respectively, $\lambda_n = c/f_n$, P_{T} is the total transmitted power, G_{T} is the TX antenna gain and G_{R} is the RX antenna gain. Note that, in an asynchronous system, t_0 and ϕ_0 are not known (*synchronization mismatch*). The random coefficient ξ_0 indicates the LOS/NLOS state of the direct path, i.e., $\xi_0 = 0$ if the direct path is obstructed (NLOS), whereas $\xi_0 = 1$ if in LOS. For what the simulation of the multipath component is concerned, we assume the widely-used L-path model

$$h_n^{(\text{mp})} = \sum_{l=1}^{L} \alpha_l \exp\left(-j2\pi f_n(\tau_l + \tau_{\text{d}} - t_0)\right) \quad (6)$$

with $\tau_{\text{d}} = \|\mathbf{p}_{\text{TX}} - \mathbf{p}\|/c$ being the TOA of the direct path, α_l and τ_l being random variables (RVs) expressing, respectively, the amplitude and delay (relative to τ_{d}) of the lth path.

The coefficient of the channel between the TX and the kth tile of the RIS for subcarrier n (kth forward channel) is

$$g_{n,k}^{(\text{r})} = g_{n,k}^{(\text{dp})} + g_{n,k}^{(\text{mp})} \quad (7)$$

with $g_{n,k}^{(\text{dp})}$ and $g_{n,k}^{(\text{mp})}$ representing the direct and multipath forward components, respectively, with the latter modeled according to the statistical model as in (6). The direct component of the kth forward channel can be written as

$$g_{n,k}^{(\text{dp})} = \xi_k \frac{\sqrt{G_{\text{T}}\,P_{\text{T}}/N_{\text{t}}}\,\lambda_n}{4\pi\|\mathbf{p}_{\text{TX}} - \mathbf{p}_k\|}$$
$$\cdot \exp\left(-j\frac{2\pi f_n}{c}\|\mathbf{p}_{\text{TX}} - \mathbf{p}_k\| + j2\pi f_n t_0 + j\phi_0\right) \quad (8)$$

where the coefficient ξ_k denotes the LOS/NLOS state of the kth forward channel. Similarly, the channel coefficient between the kth tile of the RIS and the UE for subcarrier n (kth backward channel) is

$$b_{n,k}^{(\text{r})} = b_{n,k}^{(\text{dp})} + b_{n,k}^{(\text{mp})} \quad (9)$$

with the direct backward component given by

$$b_{n,k}^{(\text{dp})} = \eta_k \frac{\sqrt{G_{\text{R}}}\,\lambda_n}{4\pi\|\mathbf{p} - \mathbf{p}_k\|} \exp\left(-j\frac{2\pi f_n}{c}\|\mathbf{p} - \mathbf{p}_k\|\right) \quad (10)$$

where η_k denotes the LOS/NLOS state of the kth backward channel. Note that (5), (8), and (10) are general as they are valid both in near- and far-field conditions. When the far-field approximation holds, for example with reference to (10), all the tiles experience the same path loss and a phase shift with constant gradient along the RIS' aperture (plane wave propagation), i.e.,

$$\exp\left(-j\frac{2\pi f_n}{c}\|\mathbf{p} - \mathbf{p}_k\|\right) \simeq \exp\left(-j\phi_{n,k}\left(\Theta^{(\text{r})}\right)\right), \quad (11)$$

where $\phi_{n,k}\left(\Theta^{(\text{r})}\right)$ depends only on the direction of the UE with respect to the RIS, i.e., the reflection angle $\Theta_k^{(\text{r})} = \Theta^{(\text{r})}\,\forall k$,

and on the spacing d among the tiles [30]. Similar considerations can be drawn for (5) and (8). As a consequence, all the tiles are subjected to the same incident/reflection angles and approximatively the same TOA measurements. On the contrary, in the near field, the incident/reflection angles of the impinging/reflected waves are different for each tile composing the RIS because the curvature of the EM wavefront is not negligible considering the size of the RIS, as already pointed out. Indeed, the TOAs of the reflected signals are in general different. The diversity among the elements of (5), (8), and (10) in the near field gives rise to the possibility to enrich the set of measurements available for positioning that will be exploited by the algorithms proposed in this paper.

Combining (7) and (9), the kth cascaded channel for sub-carrier n is given by

$$h_{n,k}^{(\text{r})} = g_{n,k}^{(\text{r})}\,b_{n,k}^{(\text{r})}. \quad (12)$$

For further convenience, we define the cascaded channel coefficient related only to the direct path components, that is,

$$h_{n,k}^{(\text{dp})} = g_{n,k}^{(\text{dp})}\,b_{n,k}^{(\text{dp})} = h_{n,k}^{(\text{dp})}(\mathbf{p}, t_0, \phi_0) \quad (13)$$

where it has been put in evidence its dependence on the unknown position $\mathbf{p}$ of the UE, and the time and phase offsets t_0 and ϕ_0, respectively.

The received signal at symbol time t and subcarrier n is given by

$$y_{n,t} = x_{n,t}\,h_n^{(\text{d})} + x_{n,t} \sum_{k=1}^{K} \beta_{t,k} h_{n,k}^{(\text{r})} + w_{n,t} \quad (14)$$

where $w_{n,t} \sim \mathcal{CN}\left(0, \sigma^2\right)$ (circular symmetric complex Gaussian RV) denotes the additive white Gaussian noise (AWGN) with power σ^2. Since the pilot symbols $\{x_{n,t}\}$ are known at the receiver, without loss of generality, in the remainder of the paper we will set $x_{n,t} = 1$, $\forall n, t$.

Starting from the measurements $\{y_{n,t}\}$, $n = 1, 2, \ldots N$, $t = 1, 2, \ldots T$, collected in T OFDM symbols and N subcarriers, the UE aims to obtain the most accurate estimate of its own position $\mathbf{p}$. The purpose is to design practical estimation algorithms, together with the phase sequences $\{\Psi_{t,k}\}$ of the RIS, which minimize the number T of required pilot symbols and/or the number N of subcarriers. Note that the overhead for positioning is given by the product $N \cdot T$, while the latency is proportional to T. Therefore, performing localization with small values of T is advantageous for both figures of merit.

III. EXTRACTION OF SIGNAL COMPONENTS

The position estimation algorithms, which will be described in Secs. IV and V, require the separation of the direct component and the components generated by the reflections from the RIS. It is worth noting that, when present, the direct path as well as the multipath components are, in general, dominant with respect to the components reflected by the RIS [17]. Consequently, special care must be taken when extracting the RIS-reflected components from the overall received signal. This process is similar to that done in UWB-RFID-based localization systems where the signal backscattered by the tag,

modulated by a time-varying sequence, has to be extracted from the received signal dominated by the clutter. To this end, the adoption of balanced sequences ensures a complete removal of the clutter [17], [18]. Thus, the RIS can be interpreted as a large set of reflecting tags whose reflection property changes dynamically according to some unique sequence.

A. Extraction of the Direct Component

The extraction of the direct component, which includes the direct link and the multipath from the environment (with the exclusion of that coming from the RIS), can be easily accomplished by designing the RIS sequences so that they result balanced when observed for $t = 1, 2, \ldots, T$ [17], [27], that is,

$$\sum_{t=1}^{T} \beta_{t,k} = 0 \qquad k = 1, 2, \ldots, K \tag{15}$$

and accumulating the received signals over T OFDM symbols as

$$y_n^{(\text{d})} = \frac{1}{T} \sum_{t=1}^{T} y_{n,t} = h_n^{(\text{dp})} + h_n^{(\text{mp})} + \sum_{k=1}^{K} h_{n,k}^{(\text{r})} \frac{1}{T} \sum_{t=1}^{T} \beta_{t,k} + \tilde{w}_n \tag{16}$$

where $\tilde{w}_n \sim \mathcal{CN}\left(0, \sigma^2\right)$. It follows that, by exploiting property (15), the third term in (16) becomes zero and hence the RIS component is completely removed thus yielding to the direct component (direct path plus multipath)

$$y_n^{(\text{d})} = h_n^{(\text{dp})} + h_n^{(\text{mp})} + \tilde{w}_n \qquad n = 1, 2, \ldots, N. \tag{17}$$

B. Extraction of the RIS Component

The RIS component can be easily isolated by simply subtracting the direct component $y_n^{(\text{d})}$ in (17) from $y_{n,t}$, which gives

$$y_{n,t}^{(\text{r})} = y_{n,t} - y_n^{(\text{d})} \qquad t = 1, 2, \ldots, T, \quad n = 1, 2, \ldots, N. \tag{18}$$

As it will be described, the positioning algorithm proposed in Sec. V requires also the knowledge of the contribution from each single tile of the RIS. To this end, the contribution of the generic tile m can be extracted by correlating $y_{n,t}^{(\text{r})}$ with the complex conjugate of the time sequence $\{\beta_{t,m}\}$ adopted by the mth tile as follows

$$u_n^{(m)} = \frac{1}{T \beta_0} \sum_{t=1}^{T} y_{n,t}^{(\text{r})} \beta_{t,m}^* \tag{19}$$

$$= h_{n,m}^{(\text{r})} \frac{1}{T \beta_0} \sum_{t=1}^{T} |\beta_{t,m}|^2 + \sum_{k \neq m} h_{n,k}^{(\text{r})} \frac{1}{T \beta_0} \sum_{t=1}^{T} \beta_{t,k} \beta_{t,m}^* + z_n$$

where $\beta_0 = N_e G_c$ is the maximum gain of the tile, and $z_n \sim \mathcal{CN}\left(0, \sigma^2\right)$, $n = 1, 2, \ldots N$. Suppose now that the RIS sequences satisfy the following orthogonality property

$$\sum_{t=1}^{T} \beta_{t,k} \beta_{t,m}^* = 0 \quad \forall k \neq m. \tag{20}$$

If property in (20) holds, then (19) reduces to

$$u_n^{(m)} = \beta_0 h_{n,m}^{(\text{r})} + z_n \tag{21}$$

and the mth component can be successfully extracted. It is worth noticing that, for very large T we have that properties (15) and (20) are approximatively satisfied using random zero mean phase sequences $\{\Psi_{t,k}\}$, according to the law of large numbers. Examples of sequences satisfying (20) when $T \geq K$ are given by the exponentials of the discrete Fourier transform (DFT) and the Hadamard codes (for the binary case) [35]. The adoption of DFT-based sequences has been investigated also in [29], [36] for CSI estimation purposes. As it will be discussed in Sec. V, when $T < K$, the orthogonality property (20) cannot be always satisfied. In such a case, inter-tile interference may arise and compromise the performance of the positioning scheme proposed, if adequate countermeasures are not taken.

In the next sections, we will illustrate two position estimation algorithms. The first aims to estimate the position directly from the extracted signal components (17) and (18) (*direct positioning*), whereas the second follows a traditional pragmatic two-step approach where, first TOA/time difference-of-arrival (TDOA) estimates are obtained from (17) and (21), then the position is computed by exploiting geometrical relationships (*two-step positioning*). It is worth noticing that regardless of the algorithm used, when operating in far-field conditions, no enough information is available to infer the UE position without ambiguities, and localization schemes designed for the far-field condition cannot be applied to single-antenna devices. In fact, the localization in far-field condition requires the availability of multiple antennas at the terminals in order to collect at least 2 angle-of-arrival (AOA) measurements, one for the BS-UE link and one for the RIS-UE link. If the BS-UE link is in NLOS, the localization is not possible even with multiple antennas (in an asynchronous system). Therefore, the proposed algorithms assume the system operates in the near-field condition, which is the typical case when working at high frequency and with large RISs, as already mentioned in Sec. I.

IV. DIRECT POSITIONING

Direct position estimation can be realized by deriving the maximum likelihood (ML) estimator of the unknown parameters $\Omega = [\mathbf{p}, t_0, \phi_0]$ (*asynchronous system*) or $\Omega = [\mathbf{p}, \phi_0]$ (*synchronous system*), through the exploitation of the model of the direct path component of the channel in (13) and the received signal component $\left\{y_{n,t}^{(\text{r})}\right\}$ in (18). Neglecting the presence of the multipath, whose effect will be accounted for in the numerical results (thus introducing a model mismatch), the log-likelihood function of the vector of measurements $\left\{y_{n,t}^{(\text{r})}\right\}$ is given by

$$f\left(\left\{y_{n,t}^{(\text{r})}\right\} | \Omega\right) = -\frac{1}{\sigma^2} \sum_{n=1}^{N} \sum_{t=1}^{T} \left| y_{n,t}^{(\text{r})} - \sum_{k=1}^{K} \beta_{t,k} h_{n,k}^{(\text{dp})}(\Omega) \right|^2 \tag{22}$$

$$= -\frac{1}{\sigma^2} \sum_{n=1}^{N} \sum_{t=1}^{T} \left| y_{n,t}^{(\text{r})} - a_{n,t}(\mathbf{p}) \exp\left(\jmath\phi_t(\mathbf{p}) + \jmath 2\pi f_n t_0 + \jmath\phi_0\right) \right|^2$$

where

$$a_{n,t}(\mathbf{p}) = \left| \sum_{k=1}^{K} \beta_{t,k} h_{n,k}^{(\text{dp})}(\Omega) \right| \tag{23}$$

and

$$\phi_t(\mathbf{p}) = \arg\left(\sum_{k=1}^{K} \beta_{t,k}\, h_{n,k}^{(\mathrm{dp})}(\Omega)\right) - 2\pi f_n t_0 - \phi_0 \qquad (24)$$

in which we took out the common terms $2\pi f_n t_0 + \phi_0$ so that $\phi_t(\mathbf{p})$ depends only on $\mathbf{p}$ and t. The ML estimate can be obtained by maximizing the log-likelihood function over the unknown parameters Ω as

$$\hat{\Omega} = \arg\max_{\Omega} f\left(\left\{y_{n,t}^{(\mathrm{r})}\right\}|\Omega\right). \qquad (25)$$

In a real scenario, the amplitude coefficients $\{a_{n,t}(\mathbf{p})\}$ could be not completely known, since this would require the perfect knowledge of the UE' orientation, the fading condition, as well as the perfect knowledge of the LOS / NLOS condition (i.e., of the coefficients $\{\xi_k\}$ and $\{\eta_k\}$). For this reason, we assume the amplitudes $\{a_{n,t}(\mathbf{p})\}$ as unknowns (i.e., nuisance parameters to be estimated, then no longer function of $\mathbf{p}$). Therefore, the log-likelihood (22) is modified as

$$f\left(\left\{y_{n,t}^{(\mathrm{r})}\right\}|\Omega, \{a_{n,t}\}\right) \qquad (26)$$

$$= -\frac{1}{\sigma^2}\sum_{n=1}^{N}\sum_{t=1}^{T}\left|y_{n,t}^{(\mathrm{r})} - a_{n,t}\exp\left(J\phi_t(\mathbf{p}) + j2\pi f_n t_0 + J\phi_0\right)\right|^2$$

where amplitudes $\{a_{n,k}\}$ are added in the list of the unknown parameters to be estimated. An analytical solution of (25) using (26) appears difficult to be found as all the optimization methods based on the derivation of the gradient cannot be used. Therefore, the simplest method to solve it is through an exhaustive search. Unfortunately, the minimization also involves t_0, ϕ_0, and the unknown amplitudes $\{a_{n,t}\}$, thus significantly augmenting the dimension of the search space and making the search not practical.

To significantly reduce the search space, a log-likelihood function independent of $\{a_{n,t}\}$ can be obtained by considering an estimate $\hat{a}_{n,t}$ of $a_{n,t}$ into (26), for any n, t, that is,

$$f\left(\left\{y_{n,t}^{(\mathrm{r})}\right\}|\Omega\right) = f\left(\left\{y_{n,t}^{(\mathrm{r})}\right\}|\Omega, \{a_{n,t}\} = \{\hat{a}_{n,t}\}\right). \qquad (27)$$

By fixing n and t, adopting again the ML criterion for the amplitude estimate, we have

$$\hat{a}_{n,t} = \arg\max_{a_{n,t}} f\left(\left\{y_{n,t}^{(\mathrm{r})}\right\}|\Omega, \{a_{n,t}\}\right)$$

$$= \arg\max_{a_{n,t}}\left(-a_{n,t}^2 + 2a_{n,t}\,\tilde{a}_{n,t}\cos\left(\tilde{\phi}_{n,t} - \phi_t(\mathbf{p}) - 2\pi f_n t_0 - \phi_0\right)\right)$$

$$= \tilde{a}_{n,t}\cos\left(\tilde{\phi}_{n,t} - \phi_t(\mathbf{p}) - 2\pi f_n t_0 - \phi_0\right) \qquad (28)$$

where $\tilde{a}_{n,t} = |y_{n,t}|$ and $\tilde{\phi}_{n,t} = \arg(y_{n,t})$ are the amplitude and argument of the observed signal $y_{n,t}$, respectively. Then, combining (26), (27), and (28), we obtain

$$f\left(\left\{y_{n,t}^{(\mathrm{r})}\right\}|\Omega\right) = -\sum_{n=1}^{N}\sum_{t=1}^{T}\frac{\tilde{a}_{n,t}^2}{\sigma^2}\sin^2\left(\tilde{\phi}_{n,t} - \phi_t(\mathbf{p}) - 2\pi f_n t_0 - \phi_0\right). \qquad (29)$$

In (29), the set of measured phase values $\{\tilde{\phi}_{n,t}\}$ is properly correlated with an hypothetical set $\{\phi_t(\mathbf{p})\}$ depending on the position $\mathbf{p}$ under test. In particular, each phase measurement is weighted by the corresponding received signal-to-noise ratio

(SNR) $\tilde{a}_{n,t}^2/\sigma^2$. In this manner, the phase values related to a larger SNR have a greater impact on the overall likelihood function and contribute heavily to the position estimation. It is worth noticing that in the derivation of the estimator, we have not considered the direct path component. Its inclusion in the derivation would have brought an additional term in (29) weighted with the SNR of the direct path which, when present, is in general much larger than the SNR of the components related to the RIS. While in theory the direct path brings additional information, the huge SNR discrepancy between the direct and RIS components could mask significantly the contribution of the RIS thus making the log-function close to being periodic[4] with the consequence of severe ambiguities in the estimation. For this reason, in (29) we consider only the contribution from the RIS.

To further reduce the search space, and hence the complexity, we propose the following modification in which N position estimates are obtained by considering each individual subcarrier separately (narrowband signals). In this case, for a fixed n, it turns out that the phase term $2\pi f_n t_0$ in (29) is fixed and it can be embedded in ϕ_0, thus obtaining

$$\hat{\mathbf{p}}^{(n)} = \arg\min_{\{\mathbf{p}, \phi_0\}}\sum_{t=1}^{T}\frac{\tilde{a}_{n,t}^2}{\sigma^2}\sin^2\left(\tilde{\phi}_{n,t} - \phi_t(\mathbf{p}) - \phi_0\right) \qquad (30)$$

for $n = 1, 2, \ldots, N$. It is worth underlining that the localization exploiting the phase profile of a narrowband signal (i.e., single-carrier) is one of the techniques used in RFID systems [37]. The difference is that here the phase profile is generated by different RIS configurations over T pilot symbols, while in RFID systems it is obtained through the observation of the signal from spatially distinct positions using different receiving antennas. The final position estimate can be obtained by taking the average of the N estimates $\{\hat{\mathbf{p}}^{(n)}\}$. However, numerical evaluations have revealed that operating like this increases the possibility that some estimates are completely wrong (outliers) because considering each subcarrier separately increases the possibility of ambiguities, i.e., many positions with similar phase profile, compared to the situation in (29) where many more terms are present in the minimization thus reducing the occurrence of ambiguities. To overcome this issue, we propose to apply an outlier removal algorithm and then to take the average considering only the residual "good" estimates, that is,

$$\hat{\mathbf{p}} = \frac{1}{P}\sum_{p\in\mathcal{P}}\hat{\mathbf{p}}^{(p)} \qquad (31)$$

where $\mathcal{P}$ is the set of elements with cardinality $P = |\mathcal{P}|$ resulting from the outlier removal procedure. The considered outlier removal procedure consists in removing all the estimates that fall outside the confidence region $[\mu_\mathrm{p} - \eta\,\sigma_\mathrm{p}, \mu_\mathrm{p} + \eta\,\sigma_\mathrm{p}]$, where μ_p and σ_p are the sample mean and standard deviation of the sequence $\{\hat{\mathbf{p}}^{(n)}\}$, respectively. Parameter η defines the width of the confidence region. A small value of η makes the outlier removal scheme more severe with the risk of discarding also good measurements, whereas a large value can result in

[4]When only one phase measurement is considered, all the locations spaced apart of a wavelength λ experience the same phase value.

outliers being included in the output set. In the numerical results, we set $\eta = 1$ obtained as a reasonable compromise from simulative investigations. In general, the reliability of the outlier removal scheme improves when the number of subcarriers is large because the sample mean and variance tend to approach the true ones.

An advantage of the proposed algorithm is that it can work both with wideband signals ($N > 1$) and narrowband signals ($N = 1$), as will be shown in the numerical results. The main drawback is the possible complexity in finding the absolute minimum in (29), especially at high frequencies, considering that the width of the minimum is of the order of λ since it is related to interfering effects of multiple components close to the central frequency. Expectation-maximization or alternating projection methods can be used to refine the search grid [38], [39].

The complexity of the direct positioning algorithm, associated with the minimization of (29) (N times), is $O(NTM)$, where M represents the number of test points in case of a brute-force minimization method is used (worst case). The choice of M depends on the desired positioning resolution Δ, the size of the search area A, and the number of test values P for ϕ_0 (in our simulation we have seen that $P = 10$ values are sufficient), specifically, $M = PA/\Delta^2$. Since the complexity is relatively independent from K (actually T is somehow related to K), this algorithm is especially suited for very large RISs, relatively small operating areas, and a small number N of subcarriers. The search area A, and hence the number of search iterations, can be greatly reduced if the estimation takes into account past estimates within a tracking process. This aspect will be the subject of a future work.

V. Two-step Positioning

In this section, we propose a two-step positioning approach in which the TOA of each signal component is estimated and then the position is inferred by leveraging on classical geometric localization schemes.

A. Estimation of the TOAs

The estimation of the TOA of the direct path (when present) can be obtained by computing the time-domain waveform from the direct component $\{y_n^{(d)}\}$ in (17) through an inverse discrete Fourier transform (IDFT) operation over the subcarrier index n

$$\left\{z_j^{(d)}\right\} = \text{IDFT}\left[\left\{y_n^{(d)}\right\}\right] \tag{32}$$

with $j = 1, 2, \ldots, J$, with $J = N F_o$ being the size of the IDFT, and F_o the oversampling factor. Once the time-domain signal $\{z_j^{(d)}\}$ is obtained, the TOA of the first arriving path can be estimated using any of the numerous algorithms present in the literature

$$\hat{\tau}_d = \text{TOA}\left[\left\{z_j^{(d)}\right\}\right] \tag{33}$$

where TOA[·] denotes any estimator of the first arriving path [40]. Among them, the simplest algorithm is that detecting the location of the highest peak.

Similarly, the contribution from the mth tile of the RIS in the time-domain can be obtained starting from the signal $\{u_n^{(m)}\}$ in (19) through the IDFT operation over the subcarrier index n

$$\left\{z_j^{(m)}\right\} = \text{IDFT}\left[\left\{u_n^{(m)}\right\}\right] \tag{34}$$

from which the TOA can be estimated

$$\hat{\tau}_m = \text{TOA}\left[\left\{z_j^{(m)}\right\}\right]. \tag{35}$$

B. Estimation of UE's Position

The TOA of the first arriving path in (33), when available and correctly detected, can be written as

$$\hat{\tau}_d = \frac{1}{c}\|\mathbf{p}_{\text{TX}} - \mathbf{p}\| - t_0 + \epsilon_d \tag{36}$$

with ϵ_d being the estimation noise. Similarly, the TOA of the component reflected by the mth tile of the RIS is

$$\hat{\tau}_m = \frac{1}{c}\|\mathbf{p}_{\text{TX}} - \mathbf{p}_m\| + \frac{1}{c}\|\mathbf{p} - \mathbf{p}_m\| - t_0 + \epsilon_m \tag{37}$$

where ϵ_m is the estimation noise. Note that the first term in (37) is known because it depends only on the position of the BS and the tiles of the RIS that are known. Since in an asynchronous system t_0 is not known, the estimation of the UE's position must be performed starting from TDOA measurements so that the common term t_0 in the previous expressions simplifies. A possible approach to form a certain number of reliable TOA couples, from which to compute TDOA values, is described in the following steps:

1) Consider only the subset of the I best TOA estimates that are reliable, i.e., corresponding to a sufficiently large SNR. Denote by $b(i)$, $i = 1, 2, \ldots I$, the index of the ith best TOA measurement

$$\hat{t}_i = \hat{\tau}_{b(i)} - \frac{1}{c}\|\mathbf{p}_{\text{TX}} - \mathbf{q}_i\| \tag{38}$$

where $\mathbf{q}_i = (x_i, y_i, z_i) = \mathbf{p}_{b(i)}$ is the coordinate of the tile of the RIS involved in the ith TOA measurement $\hat{\tau}_{b(i)}$. When the UE and the BS are in LOS, it is likely that the subset contains the TOA of the direct path between the BS and the UE. In such a case, $\mathbf{q}_i$ will be set to $\mathbf{p}_{\text{TX}}$, and $\hat{t}_i = \hat{\tau}_d$;

2) Compute $I-1$ TDOA values, $\hat{r}_i = \hat{t}_i - \hat{t}_1$, $i = 2, \ldots I$, from the $I - 1$ couples of TOA measurements with reference to the most reliable TOA estimate ($i = 1$). All the TDOA values will be independent of t_0;

3) Estimate the UE's position using any TDOA-based position estimation algorithm available in the literature. To this purpose, a simple and efficient algorithm is given by the linear least squares (LS) algorithm [41].

Regarding the complexity, it is mainly determined by the FFTs required to obtain the response in the time-domain for TOA estimation (at most $K + 1$), and the position estimation, whose complexity depends on the number of considered measurements (the best $I < K$ measurements according to our algorithm) and the specific method used to estimate the position. Thus, the overall complexity is of the order of $O\left(KNF_0 \log_2(NF_0)\right) + O\left(I^3\right)$, where the second term

accounts for the complexity of the LS-based localization method involving the inversion of a matrix of dimension $I \times I$. Compared to the direct positioning approach in Sec. IV, the proposed two-step approach is more convenient in wide area scenarios, and it is expected to be more robust in the presence of strong multipath (which leads to a model mismatch in (29)), but it works only with wideband signals (large N) to properly discriminate the first path from the multipath, and it may suffer from inter-tile interference when $T < K$. In fact, under such a condition, it is not possible to ensure that all the K RIS sequences $\{\beta_{t,k}\}$ are perfectly orthogonal to each other,[5] with the consequence that the signal components reflected by some couples of tiles may be characterized by not negligible cross-correlation. This aspect will be investigated in the numerical results. Another potential disadvantage of the two-step positioning approach is that the contribution from each tile of the RIS is considered separately from the others, then the TOA estimation algorithm does not take advantage of the SNR enhancement that would be obtained through the coherent combination of contributions from many tiles of the RIS, as intrinsically done in the direct positioning approach.

VI. PERFORMANCE BOUNDS

In this section, the derivation of the PEB on UE's position estimation error is provided as a benchmark for the algorithms proposed in the previous sections. The PEB gives the performance limit of any unbiased position estimator and it can be obtained by computing the Fisher information matrix (FIM) $\mathbf{J}(\Omega)$ associated to the parameters Ω to be estimated and the statistical model of the observations as [2], [3]

$$\mathsf{PEB} \triangleq \sqrt{\mathrm{trace}\left[\mathbf{J}^{-1}(\Omega)\right]}. \tag{39}$$

Since the two algorithms in Sec. IV (*direct positioning*) and Sec. V (*two-step positioning*) consider different observations, i.e., raw received signal and TDOA measurements, respectively, in the following we derive the FIM for the two cases.

A. PEB using raw signals

Starting from the received signals $\{y_{n,t}^{(\mathrm{r})}\}$, we define the FIM on UE's position as

$$\mathbf{J}(\Omega) \triangleq -\mathbb{E}\left\{\nabla_{\Omega}\left[\nabla_{\Omega} f\left(\{y_{n,t}^{(\mathrm{r})}\}|\Omega\right)\right]^T\right\} \tag{40}$$

where we considered $\Omega = \{\mathbf{p}\}$ by neglecting the terms due to clock or phase asynchronism, i.e., t_0, ϕ_0, thus obtaining an optimistic bound, $\nabla_{\Omega} = \left[\frac{\partial}{\partial x}, \frac{\partial}{\partial y}, \frac{\partial}{\partial z}\right]$ is the gradient operator of the position coordinates, $\mathbb{E}\{\cdot\}$ is the statistical expectation, and the log-likelihood function is obtained from (22). The generic element of the FIM in (40) is given by

$$[\mathbf{J}(\Omega)]_{i,j} = \frac{2}{\sigma^2}\Re\left\{\sum_{n=1}^{N}\sum_{t=1}^{T}\frac{\partial s_{n,t}(\Omega)}{\partial \Omega_i}\frac{\partial s_{n,t}^{*}(\Omega)}{\partial \Omega_j}\right\} \tag{41}$$

[5]The motivation behind our claim is that it is impossible to obtain K orthogonal vectors of length T when $T < K$ [35].

with $i, j = 1, 2, 3$, $s_{n,t}(\Omega) \triangleq \sum_{k=1}^{K}\beta_{t,k} h_{n,k}^{(\mathrm{dp})}(\Omega)$ is the expected received signal, and $\Omega_i \in \{x, y, z\}$. The first derivatives in (41) are given by

$$\frac{\partial s_{n,t}(\Omega)}{\partial \Omega_i} = -J\frac{2\pi}{\lambda_n}\sum_{k=1}^{K}\beta_{t,k}\, g_{n,k}\, |b_{n,k}|\exp\left(-J\frac{2\pi}{\lambda_n}d_k\right)\frac{\partial d_k}{\partial \Omega_i} \tag{42}$$

where $d_k \triangleq \|\mathbf{p} - \mathbf{p}_k\|$ is the distance of the UE and the kth tile of the RIS. The derivatives of such distances are given by

$$\frac{\partial d_k}{\partial x} = \frac{x - x_k}{d_k}, \qquad \frac{\partial d_k}{\partial y} = \frac{y - y_k}{d_k}, \qquad \frac{\partial d_k}{\partial z} = \frac{z - z_k}{d_k}. \tag{43}$$

B. PEB using TDOA measurements

Now we consider the case where the UE's position is inferred by processing an observation vector given by the best $I - 1$ TDOA estimates $\hat{\mathbf{r}} = [\hat{r}_2, \ldots, \hat{r}_i, \ldots, \hat{r}_I]^T$ obtained according to the approach proposed in Sec. V. Denote by $\mathbf{t} = [t_2, \ldots, t_i, \ldots, t_I]^T$ is the true TDOAs. A reasonable model for the measurement error variance of the TDOA estimates is given by the CRB defined as $\sigma_i^2 = \frac{1}{8\pi^2 \beta^2 \gamma_i}$, where $\beta^2 \simeq W^2$ is the squared effective bandwidth of the signal and $\gamma_i = (1/\mathsf{SNR}_i + 1/\mathsf{SNR}_1)^{-1}$ is the combined SNR of the two links involved in the TDOA estimate [40]. Given this model, the log-likelihood function is

$$f(\hat{\mathbf{r}}|\Omega) \propto -\sum_{i=2}^{I}\frac{(\hat{r}_i - t_i)^2}{2\,\sigma_i^2}. \tag{44}$$

Therefore, the FIM can be derived as

$$\mathbf{J}(\Omega) = \mathbb{E}\left\{\nabla_{\Omega}^T f(\hat{\mathbf{r}}|\Omega)\,\nabla_{\Omega} f(\hat{\mathbf{r}}|\Omega)\right\} = \sum_{i=2}^{I}\frac{1}{\sigma_i^2}\nabla_{\Omega}^T t_i\,\nabla_{\Omega} t_i \tag{45}$$

where $\nabla_{\Omega} t_i = \left[\frac{\partial t_i}{\partial x}, \frac{\partial t_i}{\partial y}, \frac{\partial t_i}{\partial z}\right]$ is the gradient of TDOAs, with elements given by

$$\begin{aligned} \frac{\partial t_i}{\partial x} &= \frac{x - x_i}{c\, d_i} - \frac{x - x_1}{c\, d_1} \\ \frac{\partial t_i}{\partial y} &= \frac{y - y_i}{c\, d_i} - \frac{y - y_1}{c\, d_1} \\ \frac{\partial t_i}{\partial z} &= \frac{z - z_i}{c\, d_i} - \frac{z - z_1}{c\, d_1}. \end{aligned} \tag{46}$$

VII. NUMERICAL RESULTS

A. Case Study

This section presents some numerical results obtained using the parameters summarized in Table I, unless otherwise specified. The considered scenario is represented in Fig. 1, where a linear RIS of $K = 100$ tiles, with tile spacing $d = 20\,\mathrm{cm}$ is distributed along two adjacent walls of side $10\,\mathrm{m}$ at the height of $3\,\mathrm{m}$. More precisely, the linear RIS develops from coordinate $(-5, 0, 3)\,\mathrm{m}$ to coordinate $(5, 0, 3)\,\mathrm{m}$ (first wall), and from coordinate $(5, 0, 3)\,\mathrm{m}$ to coordinate $(5, 10, 3)\,\mathrm{m}$ (second wall). The BS is located in position $\mathbf{p}_{\mathrm{TX}} = (0, 5, 3)\,\mathrm{m}$, whereas the UE is randomly located with uniform distribution in the area $(-4, 1, 1) \times (4, 10, 1)\,\mathrm{m}^2$. We consider the most challenging and interesting scenario where the BS and UE are always in

Parameter	Symbol	Value
Carrier frequency	f_c	3.5-28 GHz
TX antenna gain	G_T	6 dB
RX antenna gain	G_R	2 dB
Total number of subcarriers	N_t	2048
Pilot subcarriers	N	1-2048
Subcarrier bandwidth	Δf	120 kHz
TX power per subcarrier	P_T/N_t	-5 dBm
TX-RX clock uncertainty	T_a	100 ns
UE noise figure	n_f	3 dB
Noise power	$\sigma^2 = \kappa\,290\,n_f\,\Delta f$	-120.2 dBm
Boltzmann constant	κ	$1.38 \cdot 10^{-23}$ J/K
DFT oversampling factor	F_o	8
DFT size	$J = F_o \cdot N$	$8 \times N$
NLOS Path-loss exponent	n_e	3
Delay spread	S_τ	20 ns
Number of paths	L	10
Path arrival rate	T_τ	8 ns
RIS cells per tile	$N_x \times N_y = N_e$	$4 \times 25 = 100$
Cell size	L_x, L_y	$\lambda/2, \lambda/2$
RIS tiles spacing	d	20 cm
RIS number of tiles	K	100 tiles

Fig. 2. Average localization error with the direct positioning algorithm. Random uniform RIS sequences.

NLOS, i.e., $\xi_0 = 0$, so that the localization relies only on the signals reflected by the RIS. Results refer to an asynchronous system in which we model the clock and phase offsets t_0 and ϕ_0 as RVs uniformly distributed in $[0, T_a]$ and $[0, 2\pi]$, respectively, where T_a denotes the clock mismatch uncertainty.

The statistical model in (6) is considered for the simulations with the following parameters: τ_l are drawn from RVs distributed according to a Poisson point process with arrival rate T_τ; $\alpha_l \sim \mathcal{CN}(0, \Lambda_l)$, with $\{\Lambda_l\}$ being the power delay profile. The power delay profile is modeled according to the one-sided exponential function, i.e., $\Lambda_l = \frac{\Lambda_0}{S} \exp\left(-\frac{\tau_l}{S_\tau}\right)$, for $l = 1, 2, \ldots, L$, with $S = \sum_l \exp\left(-\frac{\tau_l}{S_\tau}\right)$, and S_τ being the delay spread. Λ_0 is the distant-dependent path-loss gain of the NLOS component, where $\Lambda_0\,(\text{dB}) = -\text{PL}_0 - 10\,n_e \log_{10} d$, with PL_0 denoting the path-loss (in dB) at the reference distance of one meter, d the distance between the considered devices, and n_e the path-loss exponent [42].

Regarding the RIS sequences, we consider the following choices: (i) *Random uniform*: Reflection phases $\{\Psi_{t,k}\}$ uniformly and independently distributed in $[0, 2\pi]$; (ii) *Random binary*: Independent random reflection phases $\{\Psi_{t,k}\}$ taking the values $\{0, \pi\}$ with identical probability; (iii) *DFT*: Reflection phases $\{\Psi_{t,k}\}$ designed as follows

$$\Psi_{t,k} = \frac{2\pi\,k\,t}{T} \quad t = 1, 2, \ldots T, \quad k = 1, 2, \ldots, K \quad (47)$$

which give perfectly orthogonal balanced sequences when $T > K$. As will become evident later, the inter-tile interference arising when $T \leq K$ can be significantly mitigated by considering the following modified DFT-based phase sequences

$$\Psi_{t,k} = \frac{2\pi\,t\,\lfloor k\,T/K \rfloor}{T} \quad t = 1, 2, \ldots T, \quad k = 1, 2, \ldots, K \quad (48)$$

with $\lfloor x \rfloor$ returning the largest integer smaller than x, which corresponds to assigning the same sequence to adjacent tiles so that inter-tile interference will result into a small TOA estimation error.
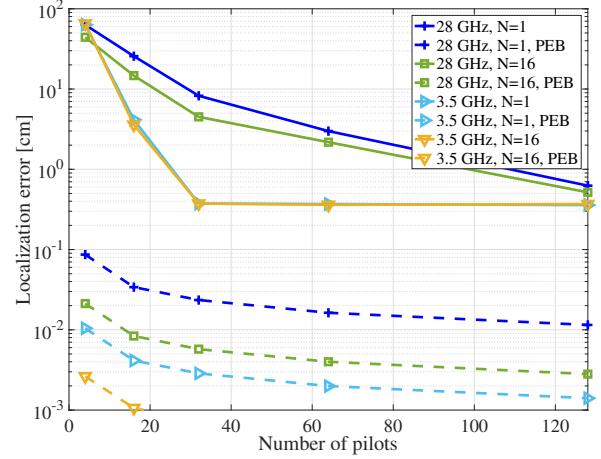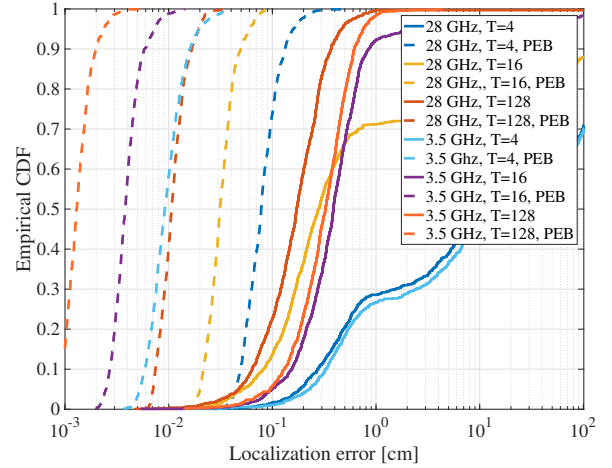

Fig. 3. Empirical CDF of the localization error with the direct positioning algorithm. $N = 1$, random uniform RIS sequences.

B. Direct Positioning

We first examine the localization performance of the direct positioning algorithm. Fig. 2 shows the localization error averaged over 1000 Monte Carlo iterations as a function of the number T of pilot OFDM symbols, assuming random uniform RIS sequences. Curves for a different number of subcarriers and carrier frequencies, i.e., $f_c = 28\,\text{GHz}$ and $f_c = 3.5\,\text{GHz}$, are reported. Interestingly, relatively high-accuracy localization can be achieved even using few or only one subcarrier (narrowband localization) as long as a sufficient number of pilot symbols are transmitted (higher latency). On the other hand, when using a relatively large number of subcarriers (wideband localization), very high localization accuracy with errors even below 1 cm can be achieved using a reduced number of pilot symbols, and thus resulting in lower latency. These results put in evidence the possibility to localize the UE with only one anchor node (the BS) in NLOS condition by exploiting only the reflections from the RIS. The PEB is also reported for each configuration. As expected,
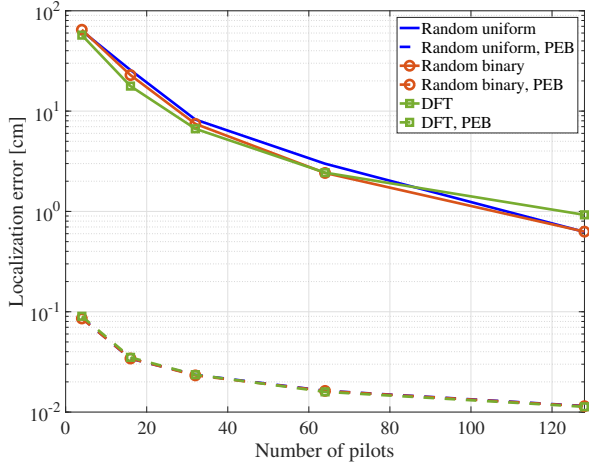
Fig. 4. Average localization error with the direct positioning algorithm for different RIS sequences. f_c = 28 GHz, N = 1. PEB curves are overlapped.
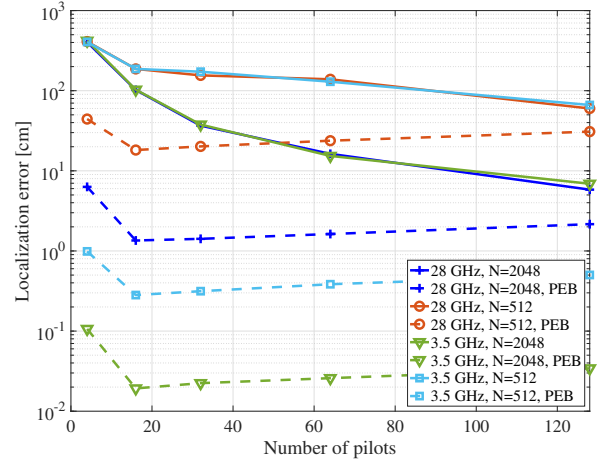

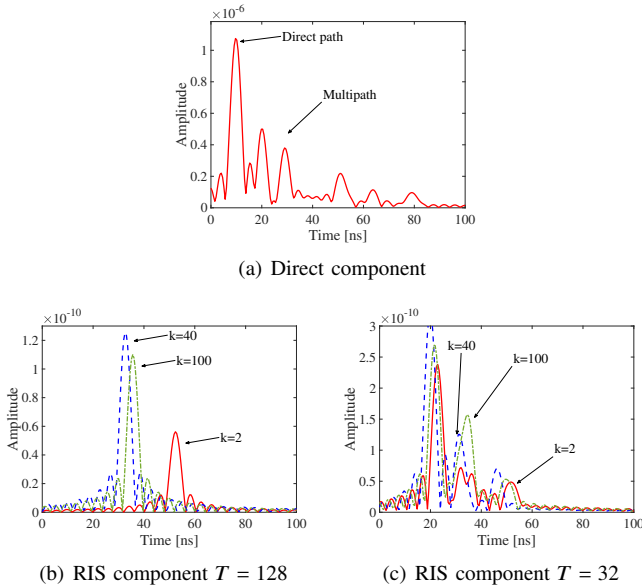Fig. 6. Average localization error with the two-step positioning algorithm. DFT RIS sequences (48).

(a) Direct component

(b) RIS component T = 128

(c) RIS component T = 32

Fig. 5. Extracted components for f_c = 28 GHz, N = 2048, and DFT RIS sequences (47). The UE is located at $\mathbf{p}$ = (4, 5, 1) m.

Fig. 7. Localization error with the two-step positioning algorithm. N = 2048, DFT RIS sequences (48).

when increasing N and T, the PEB decreases. Moreover, we assist to a decrease of the PEB also when lowering the carrier frequency, which can be ascribed to the more favorable path loss. Vice-versa, the performance of the direct positioning algorithm exhibits a floor when increasing N, T and decreasing the carrier frequency, which is quite far from the theoretical bound. Such a floor is due to the resolution limit $\Delta = 0.1$ cm imposed by the search algorithm, and hence on the number of searches M that has to be kept to a reasonable level to avoid an explosion of complexity. Obviously, the performance can be traded with complexity through M.

In Fig. 3, the empirical cumulative distribution function (CDF) of the localization error for N = 1 is shown for different values of T and for carrier frequencies f_c = 3.5 GHz and f_c = 28 GHz. This plot highlights an "on-off" behavior of the algorithm when N and T are small, evidenced by the presence
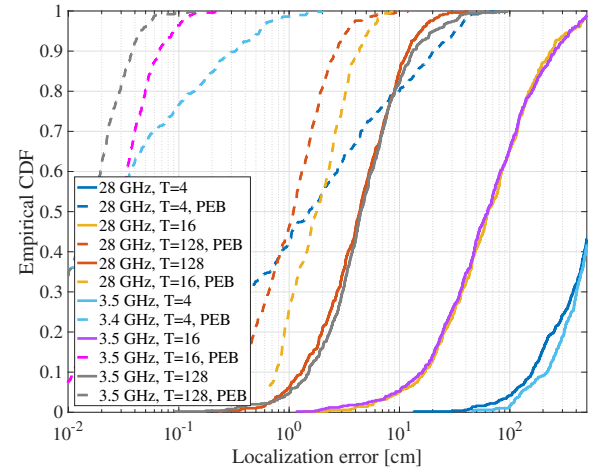
of horizontal asymptotes and symptomatic of the presence of some locations where positioning is not possible due to scarce SNR and the presence of outliers, i.e., strong ambiguities in the likelihood function. This phenomenon is slightly alleviated by lowering the center frequency which corresponds to a less severe path loss. In general, the coverage can be ameliorated by increasing T and/or N, as it can be also deduced from Fig. 2.

The impact of different RIS sequences, respectively, random uniform, random binary, and DFT, is investigated in Fig. 4 obtained for N = 1. Results show that, with the direct positioning algorithm, the choice of RIS sequences is not critical as long as they satisfy (15), at least approximately.

C. Two-step Positioning

The two-step positioning algorithm leverages on the correct separation of signal components. In Figs. 5(a) and 5(b), examples of extracted direct and RIS-reflected components are shown, respectively, using DFT-based sequences with T = 128
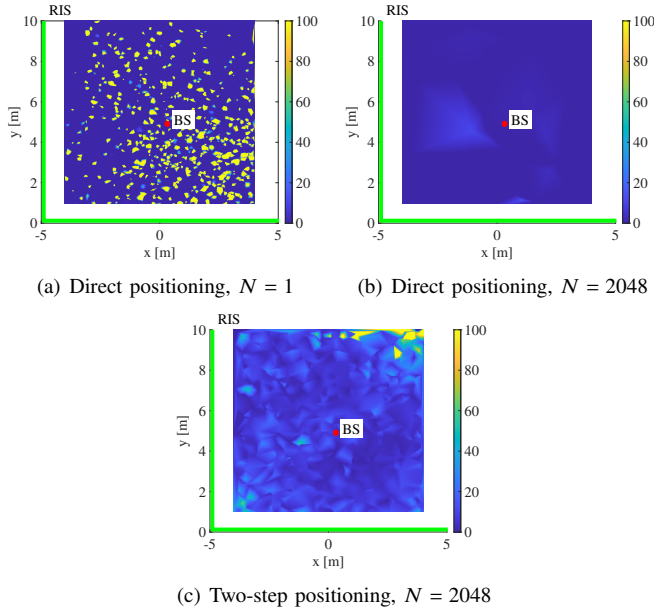
(a) Direct positioning, $N = 1$

(b) Direct positioning, $N = 2048$

(c) Two-step positioning, $N = 2048$

Fig. 8. Localization error heat maps (in cm). $T = 128$.

(a) Direct positioning

(b) Two-step positioning

Fig. 9. Localization error evolution for different NLOS duty cycle. $N = 2048$, $T = 128$.

and considering the UE located in a fixed LOS condition with respect to the BS. The direct component contains the direct path and the multipath, as evidenced in Fig. 5(a), where the components reflected by the RIS are completely eliminated thanks to property (15). The orthogonality of the DFT sequences for all tiles ensures that the signal component reflected by each individual tile can be isolated together with the corresponding multipath, as shown in Fig. 5(b) for some tiles. This is no longer true if $T < K$, as it can be noticed in Fig. 5(c) obtained by setting $T = 32$ and using the DFT phase sequences in (47), where the extracted components are dominated by the components caused by tiles whose sequence has a high cross-correlation with the useful one and are subjected to a more favorable path loss. This phenomenon can lead to a completely wrong TOA estimation in the two-step positioning algorithm. For this reason, the following numerical results have been obtained by adopting the modified DFT in (48), which keeps the tiles with highly correlated sequences close to each other, thus minimizing the error in TOA estimation in case of wrong peak detection.

The performance of the two-step positioning algorithm can be appreciated in Fig. 6, where the average localization error as a function of T and for different number of subcarriers and carrier frequencies is reported. The modified DFT sequences in (48) are used and the NLOS condition is considered ($\xi_0 = 0$). The TOA measurements with SNR > 10 dB among the $I = 3/4K$ best TOA measurements are selected and used to form $I - 1$ TDOA couples. Compared to the performance obtained with the direct positioning approach in Fig. 2, it can be noticed that the performance is worse because with the two-step approach the SNR gain from a coherent combination of all the reflected signals is not exploited. Moreover, as soon as N decreases, the performance drops significantly because the TOA estimation accuracy is limited by the inverse of the signal bandwidth, as indicated by the theoretical analysis in Sec.
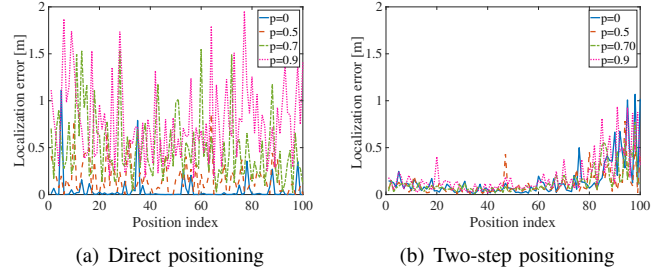
VI, and the reduced time resolution does not allow sufficient discrimination of the first path from the multipath [40]. This confirms that this approach is suitable for wideband signals only and that the performance is theoretically dominated by signal bandwidth (see PEB curves) even though also the two-step algorithm presents a performance floor dictated by the DFT resolution, i.e., the oversampling factor F_0. Nevertheless, a localization accuracy better than 10 cm is obtained in more than 90% of cases with $T = 128$, as it can be observed from the empirical CDF in Fig. 7.

Figs. 8(a)-(c) show the localization heat maps for the direct positioning and the two-step positioning in order to get an idea of how the localization error is distributed within the area of interest. The "on-off" behavior of the first algorithm is evident in Fig. 8(a) obtained with $N = 1$, whereas it can be completely removed using large N, as it can be noticed in Fig. 8(b), but at the expense of much higher complexity. On the other hand, the two-step positioning algorithm, depicted in Fig. 8(c), provides a good trade-off between performance and complexity.

D. Soft-coverage Analysis

Finally, in Figs. 9(a) and 9(b), the effect of partial RIS obstruction is investigated for the direct and two-step positioning algorithms, respectively. Here the UE was supposed to move in a straight line in 100 test locations from coordinate $(-4, 1, 1)$ m to the coordinate $(4, 10, 1)$ m, always in NLOS with respect to the BS, and the tiles of the RIS were periodically in NLOS condition, i.e., $\eta_k = 0$, with respect to the UE, with spatial period of 2 m and duty cycle p. The plots, derived for increasing values of p, show that the direct positioning algorithm appears relatively sensitive to partial RIS obstructions, especially when $p > 50\%$, due to a significant increase of outliers caused by model mismatch (the estimator in (25) and (29) is unaware that several contributions are missing). This effect could be mitigated by resorting to tracking methods based, for instance, on Bayesian filtering tools [43]. By contrast, the two-step algorithm in Fig. 9(b) exhibits the soft-coverage property. In particular, it can be noticed that when 70% of the tiles of the RIS are obstructed, the performance degradation is still negligible. Even with 90% of obstructed tiles, it is possible to localize with an accuracy of about 25 cm or less in most locations without abrupt performance degradation.

VIII. Conclusion

In this paper, we have proposed two localization algorithms aided by the presence of a large RIS to allow mobile asynchronous UEs localize themselves through the processing, over a certain number of pilot symbols, of the downlink OFDM signal emitted by one reference BS (anchor node). By a proper design of the time-varying reflection coefficients of the RIS, it has been shown that, thanks to the large size of the RIS, it is possible to localize the UE with only one BS under NLOS conditions exploiting the reflections from the RIS, making the proposed algorithms particularly interesting in applications characterized by harsh propagation conditions and coverage issues. It is worth pointing out that the time-varying configuration of the RIS does not depend on the number of UEs so that our scheme can work with a potentially unlimited number of UEs without additional overhead and signaling.

In the numerical results, the two localization algorithms have been compared in terms of performance and trade-off between bandwidth, overhead, operating frequency, latency, and complexity. Specifically, the direct positioning algorithm provides the highest accuracy, in the order of the wavelength, and allows both narrowband and wideband localization. Narrowband localization entails a higher latency than wideband localization, which in turn is more sensitive to the presence of outliers. On the other hand, the two-step algorithm only works with wideband signals and offers localization accuracy inversely proportional to the signal bandwidth as well as better robustness to outliers than the direct positioning algorithm. The soft-coverage capability of the two-step algorithm, when considering a large linear RIS and, hence, exploiting near-field propagation conditions, has been demonstrated by verifying the possibility of maintaining high localization accuracy in the presence of increasing levels of obstruction of the RIS. Future works will be addressed to the design and study of tracking schemes that can further improve the performance by reducing the occurrence of outliers as well as the exploitation of multiple antennas at BS and UE sides.

References

[1] C. De Lima, D. Belot, R. Berkvens, A. Bourdoux, D. Dardari, M. Guillaud, M. Isomursu, E. S. Lohan, Y. Miao, A. N. Barreto, M. R. K. Aziz, J. Saloranta, T. Sanguanpuak, H. Sarieddeen, G. Seco-Granados, J. Suutala, T. Svensson, M. Valkama, B. Van Liempd, and H. Wymeersch, "Convergent communication, sensing and localization in 6G systems: An overview of technologies, opportunities and challenges," *IEEE Access*, vol. 9, pp. 26 902–26 925, 2021.

[2] M. Z. Win, A. Conti, S. Mazuelas, Y. Shen, W. M. Gifford, D. Dardari, and M. Chiani, "Network localization and navigation via cooperation," *IEEE Commun. Mag.*, pp. 56–62, May 2011.

[3] M. Z. Win, Y. Shen, and W. Dai, "A theoretical foundation of network localization and navigation," *Proc. IEEE*, vol. 106, no. 7, pp. 1136–1165, Jul. 2018, special issue on *Foundations and Trends in Localization Technologies*.

[4] M. Z. Win, W. Dai, Y. Shen, G. Chrisikos, and H. V. Poor, "Network operation strategies for efficient localization and navigation," *Proc. IEEE*, vol. 106, no. 7, pp. 1224–1254, Jul. 2018, special issue on *Foundations and Trends in Localization Technologies*.

[5] H. Sarieddeen, N. Saeed, T. Y. Al-Naffouri, and M. Alouini, "Next generation Terahertz communications: A rendezvous of sensing, imaging, and localization," *IEEE Commun. Mag.*, vol. 58, no. 5, pp. 69–75, May 2020.

[6] S. Hu, F. Rusek, and O. Edfors, "Beyond massive MIMO: The potential of positioning with large intelligent surfaces," *IEEE Trans. Signal Processing*, vol. 66, no. 7, pp. 1761–1774, Apr. 2018.

[7] F. Guidi and D. Dardari, "Radio positioning with EM processing of the spherical wavefront," *IEEE Trans. Wireless Commun.*, vol. 20, no. 6, pp. 3571–3586, 2021.

[8] A. Guerra, F. Guidi, and D. Dardari, "Single-anchor localization and orientation performance limits using massive arrays: MIMO vs. beamforming," *IEEE Trans. Wireless Commun.*, vol. 17, no. 8, pp. 5241–5255, Aug. 2018.

[9] B. Friedlander, "Localization of signals in the near-field of an antenna array," *IEEE Trans. Signal Processing*, vol. 67, no. 15, pp. 3885–3893, Aug. 2019.

[10] A. Guerra, F. Guidi, D. Dardari, and P. M. Djuric, "Near-field tracking with large antenna arrays: Fundamental limits and practical algorithms," *IEEE Trans. Signal Process.*, vol. 69, pp. 5723–5738, 2021.

[11] Z. Abu-Shaban, K. Keykhosravi, M. F. Keskin, G. C. Alexandropoulos, G. Seco-Granados, and H. Wymeersch, "Near-field localization with a reconfigurable intelligent surface acting as lens," in *ICC 2021 - IEEE International Conference on Communications*, 2021, pp. 1–6.

[12] H. Wymeersch, J. He, B. Denis, A. Clemente, and M. Juntti, "Radio localization and mapping with reconfigurable intelligent surfaces: Challenges, opportunities, and research directions," *IEEE Vehicular Technology Mag.*, vol. 15, no. 4, pp. 52–61, Dec 2020.

[13] N. Decarli, A. Guerra, A. Conti, R. D'Errico, A. Sibille, and D. Dardari, "Non-regenerative relaying for network localization," *IEEE Trans. Wireless Commun.*, vol. 13, no. 1, pp. 174–185, Jan. 2014.

[14] E. Leitinger, P. Meissner, C. Rüdisser, G. Dumphart, and K. Witrisal, "Evaluation of position-related information in multipath components for indoor positioning," *IEEE J. Select. Areas Commun.*, vol. 33, no. 11, pp. 2313–2328, Nov. 2015.

[15] K. Witrisal, P. Meissner, E. Leitinger, Y. Shen, C. Gustafson, F. Tufvesson, K. Haneda, D. Dardari, A. F. Molisch, A. Conti, and M. Z. Win, "High-accuracy localization for assisted living: 5G systems will turn multipath channels from foe to friend," *IEEE Signal Processing Mag.*, vol. 33, no. 2, pp. 59–70, Mar. 2016. [Online]. Available: http://ieeexplore.ieee.org/abstract/document/7426565/

[16] E. Leitinger, F. Meyer, F. Hlawatsch, K. Witrisal, F. Tufvesson, and M. Z. Win, "A belief propagation algorithm for multipath-based SLAM," *IEEE Trans. Wireless Commun.*, vol. 18, no. 12, pp. 5613–5629, Dec 2019.

[17] D. Dardari, R. D'Errico, C. Roblin, A. Sibille, and M. Z. Win, "Ultrawide bandwidth RFID: The next generation?" *Proc. IEEE*, vol. 98, no. 9, pp. 1570 –1582, Sep 2010, special Issue on RFID - A Unique Radio Innovation for the 21st Century.

[18] N. Decarli, F. Guidi, and D. Dardari, "A novel joint RFID and radar sensor network for passive localization: Design and performance bounds," *IEEE J. Select. Topics Signal Processing*, vol. 8, no. 1, pp. 80–95, Feb. 2014, special Issue on Non-cooperative Localization Networks.

[19] A. Costanzo, D. Dardari, J. Aleksandravicius, N. Decarli, M. D. Prete, D. Fabbri, M. Fantuzzi, A. Guerra, D. Masotti, M. Pizzotti, and A. Romani, "Energy autonomous UWB localization," *IEEE Journal of Radio Frequency Identification*, vol. 1, no. 3, pp. 228–244, Sept 2017.

[20] A. Elzanaty, A. Guerra, F. Guidi, and M.-S. Alouini, "Reconfigurable intelligent surfaces for localization: Position and orientation error bounds," *IEEE Trans. Signal Process.*, vol. 69, pp. 5386–5402, 2021.

[21] T. Ma, Y. Xiao, X. Lei, W. Xiong, and Y. Ding, "Indoor localization with reconfigurable intelligent surface," *IEEE Communications Letters*, vol. 25, no. 1, pp. 161–165, Jan 2021.

[22] H. Wymeersch and B. Denis, "Beyond 5G wireless localization with reconfigurable intelligent surfaces," in *ICC 2020 - 2020 IEEE International Conference on Communications (ICC)*, June 2020, pp. 1–6.

[23] J. He, H. Wymeersch, L. Kong, O. Silvn, and M. Juntti, "Large intelligent surface for positioning in millimeter wave MIMO systems," in *2020 IEEE 91st Vehicular Technology Conference (VTC2020-Spring)*, May 2020, pp. 1–5.

[24] H. Zhang, H. Zhang, B. Di, K. Bian, Z. Han, and L. Song, "Metalocalization: Reconfigurable intelligent surface aided multi-user wireless indoor localization," *IEEE Trans. Wireless Commun.*, pp. 1–1, 2021.

[25] ——, "Towards ubiquitous positioning by leveraging reconfigurable intelligent surface," *IEEE Communications Letters*, vol. 25, no. 1, pp. 284–288, Jan 2021.

[26] C. L. Nguyen, O. Georgiou, and G. Gradoni, "Reconfigurable Intelligent Surfaces and Machine Learning for Wireless Fingerprinting Localization," *arXiv e-prints*, p. arXiv:2010.03251, Oct. 2020.

[27] K. Keykhosravi, M. Furkan Keskin, G. Seco-Granados, and H. Wymeersch, "SISO RIS-enabled joint 3D downlink localization and synchronization," in *IEEE Int. Conf. Commun.*, 2021, pp. 1–6.

[28] E. Björnson, H. Wymeersch, B. Matthiesen, P. Popovski, L. Sanguinetti, and E. de Carvalho, "Reconfigurable Intelligent Surfaces: A Signal

Processing Perspective With Wireless Applications," *arXiv e-prints*, p. arXiv:2102.00742, Feb. 2021.

[29] C. You, B. Zheng, and R. Zhang, "Intelligent reflecting surface with discrete phase shifts: Channel estimation and passive beamforming," in *ICC 2020 - 2020 IEEE International Conference on Communications (ICC)*, June 2020, pp. 1–6.

[30] C. A. Balanis, *Antenna Theory: analysis and design*. New Jersey, USA: Wiley, 2016.

[31] M. Najafi, V. Jamali, R. Schober, and H. V. Poor, "Physics-based modeling and scalable optimization of large intelligent reflecting surfaces," *IEEE Transactions on Communications*, vol. 69, no. 4, pp. 2673–2691, 2021.

[32] W. Tang, M. Z. Chen, X. Chen, J. Y. Dai, Y. Han, M. Di Renzo, Y. Zeng, S. Jin, Q. Cheng, and T. J. Cui, "Wireless communications with reconfigurable intelligent surface: Path loss modeling and experimental measurement," *IEEE Transactions on Wireless Communications*, vol. 20, no. 1, pp. 421–439, Jan 2021.

[33] S. W. Ellingson, "Path Loss in Reconfigurable Intelligent Surface-Enabled Channels," *arXiv e-prints*, p. arXiv:1912.06759, Dec. 2019.

[34] D. Dardari and D. Massari, "Using metaprisms for performance improvement in wireless communications," *IEEE Trans. Wireless Commun.*, vol. 20, no. 5, pp. 3295–3307, 2021.

[35] A. J. Viterbi, *CDMA: Principles of Spread Spectrum Communication*, 1st ed. Reading, MA: Addison-Wesley, 1995.

[36] T. L. Jensen and E. De Carvalho, "An optimal channel estimation scheme for intelligent reflecting surfaces based on a minimum variance unbiased estimator," in *ICASSP 2020 - 2020 IEEE International Conference on Acoustics, Speech and Signal Processing (ICASSP)*, 2020, pp. 5000–5004.

[37] N. Decarli, "On phase-based localization with narrowband backscatter signals," *EURASIP J. Adv. Signal Process.*, vol. 2018, no. 70, 2018.

[38] E. Tzoreff and A. J. Weiss, "Expectation-maximization algorithm for direct position determination," *Signal Processing, Elsevier*, vol. 133, pp. 32–39, 2017. [Online]. Available: https://www.sciencedirect.com/science/article/pii/S0165168416302821

[39] M. Oispuu and U. Nickel, "Direct detection and position determination of multiple sources with intermittent emission," *Signal Processing, Elsevier*, vol. 90, no. 12, pp. 3056–3064, 2010.

[40] D. Dardari, A. Conti, U. Ferner, A. Giorgetti, and M. Z. Win, "Ranging with ultrawide bandwidth signals in multipath environments," *Proc. IEEE*, vol. 97, no. 2, pp. 404–426, Feb 2009, special Issue on UWB Technology & Emerging Applications.

[41] W. Peng, S. Shaojing, Z. Zhen, G. Xiaojun, S. Bei, and W. Xudong, "Time Difference of Arrival (TDoA) Localization Combining Weighted Least Squares and Firefly Algorithm," *Sensors 19*, no. 11:2554, 2019.

[42] A. F. Molisch, *Wireless Communications*, 2nd ed. United Kingdom: IEEE Press, John Wiley & Sons Ltd., 2010.

[43] D. Dardari, P. Closas, and P. M. Djuric, "Indoor tracking: Theory, methods, and technologies," *IEEE Trans. Veh. Technol.*, vol. 64, no. 4, pp. 1263–1278, April 2015.